

# Robust Vehicle Sideslip Angle Estimation through a Disturbance Rejection Filter that Integrates a Magnetometer with GPS

Jong-Hwa Yoon and Huei Peng

**Abstract**— This paper presents a novel method which estimates the vehicle sideslip angle for a wide range of surface frictions and road bank angles by combining measurements of a magnetometer, Global Positioning System (GPS), and Inertial Measurement Unit (IMU). To reject disturbances in the magnetometer, a new stochastic filter is designed and integrated on the Kalman Filter framework. The significant latency in a low-cost GPS velocity measurement is addressed by “measurement shifting”, and biases in the IMU measurements are estimated through state augmentation. Dual Kalman Filters are employed in the sensor fusing framework. A comprehensive simulation study was conducted to prove the feasibility of the method. Finally, the performance and accuracy are verified through extensive experiments.

**Index Terms**—Sideslip estimation, magnetometer, stochastic filter, disturbance rejection, Global Positioning System (GPS), Kalman Filter

## I. INTRODUCTION

THE vehicle sideslip angle is a critical piece of information for electronic stability control (ESC) systems; hence the National Highway Traffic Safety Administration (NHTSA) sets its estimation as a requirement of production ESC in the United States. Many researchers have proposed methodologies toward its estimation, which can be grouped into three categories; Dynamic model-based, IMU integration-based, and GPS-based.

Dynamic model-based methods employ a vehicle dynamic model that describes how the estimated sideslip angle is affected by and related to vehicle input signals and parameters, such as steering angle and tire cornering stiffness. Farrelly [1] proposed a standard Luenberger observer of a linearized system with Kalman Filter gains and Insensitive Observer gains. Kalman Filter gains are selected for optimal noise rejection, and the Insensitive Observer gain is selected to enhance robustness against parameter uncertainties. Kiencke [2] showed the feasibility of a nonlinear observer and the nonlinear observer was found to outperform the linear observer in his work. Best [3] showed that simultaneous estimation of cornering stiffness enhanced sideslip angle estimation performance. Stephan [4] compared the estimation

performance of four types of observers (linear observer, extended Luenberger observer, extended Kalman filter, and sliding-mode observer), and concluded that nonlinear observers worked better than linear observers. Cherouat [5] also proposed a nonlinear observer which does not require yaw rate measurement. Yih [6] proposed to use steering torque information for sideslip angle estimation. This method would be useful for steer-by-wire systems. Gao [7] showed that a high-gain observer based on input-output linearization was useful. Grip [8] proposed a nonlinear observer with friction adaptation. Dynamic model-based methods have shown the capability to estimate sideslip angles. However, this class of methods has two drawbacks; it requires accurate vehicle parameter information such as cornering stiffness, vehicle mass and moment of inertia [1, 9], and they work only for small sideslip angles (roughly 4 degree or less) [10].

IMU integration-based methods process signals of the Inertial Measurement Unit (IMU) to estimate the sideslip angle. Farrelly was among the early researchers to use this method [1]. He showed that sideslip estimation was robust to cornering stiffness variations. It was also shown that the method worked for large sideslip angle, which is in the nonlinear range of the sideslip-lateral force curve. Imsland [11] proposed a nonlinear observer and showed that the estimation performance was satisfactory even at large sideslip angles. Ungoren [12] also confirmed the robustness of IMU integration-based methods for various sideslip angle ranges. This type of method does not require accurate parameters and works well even for large sideslip angles. However, unknown bias in the sensor measurement can significantly deteriorate the estimation accuracy because IMU integration-based methods heavily rely on measurement integration.

Bevly proposed a method utilizing a single antenna GPS along with an IMU for sideslip angle estimation [13-14]. Since the vehicle heading angle is not observable with a single antenna GPS, this method relies on IMU measurement integration to calculate the heading angle. Even though this method demonstrated its estimation capability, it does not effectively address out-of-plane vehicle motion such as roll and pitch angles. Yoon proposed a new method using two single antenna GPS receivers [15]. This method uses the kinematic relationship between the velocities of two GPS receivers; hence vehicle heading and sideslip angles are calculated directly. However, this method works only for in-plane vehicle motion. Ryu proposed a method using a dual-

J.-H. Yoon and H.Peng are with the Department of Mechanical Engineering, G041 Lay Automotive Laboratory, University of Michigan, Ann Arbor, MI 48109 USA (e-mail: [jongy@umich.edu](mailto:jongy@umich.edu); [hpeng@umich.edu](mailto:hpeng@umich.edu))

antenna GPS receiver [16-18]. In his work, the vehicle heading angle is directly measured by detecting the phase shift of carrier waves arriving at two different antennae at known locations on the vehicle. This method can provide very accurate sideslip estimations on various frictional surfaces, even on banked roads. However, it is too expensive to be used in production vehicles today[9].

This paper proposes a new method to estimate the vehicle sideslip angle for a wide range of road surface frictions and bank angles. This method combines measurements of the velocity from a single antenna GPS, local magnetic fields from a magnetometer and angular-velocity/acceleration from an IMU. Even though magnetometer measurements contain information of vehicle heading angle, using it for a ground vehicle application is not common due to its high susceptibility to disturbances [19]. This paper introduces a stochastic filter to reject large errors in magnetometer measurements and it is integrated on a Kalman filter framework. We also present a method addressing delays in GPS measurements. This is important because low-cost GPS receivers are known to have significant delays partly due to their low update rates (< 5 Hz)[16-17]. This method has much lower integration cost than the dual antenna GPS receiver based method. Details are presented in the discussion section.

The remainder of this paper is organized as follows. Section II describes principles of a disturbance rejecting stochastic filter and its integration on the Kalman Filter framework. Section III discusses serial Kalman Filters for sideslip estimation. The modified Kalman Filter of Section II is applied here. Section IV discusses the stochastic observability of the Kalman Filter and justifies use of the bicycle model during straight driving. Section V shows results of a comprehensive simulation study using the commercial software CarSim<sup>TM</sup>. Section VI presents results of experimental verification and discusses the performance in a statistical context. Discussions are presented in Section VII.

## II. A DISTURBANCE REJECTING STOCHASTIC FILTER

### A. Attitude measurement by a magnetometer

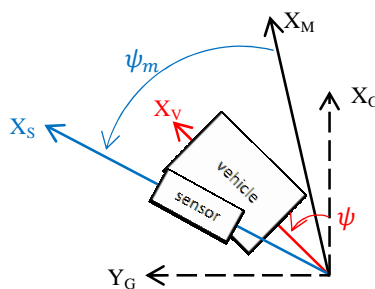


Fig. 1 Top view of four coordinate frames

Fig. 1 shows four sets of coordinate frames employed in this study. In the figure, the frame with the subscript ‘G’ represents the geographic Earth-fixed frame (G-frame).  $X_G$  and  $Y_G$  point to the geographic North and West, respectively. The frame of a subscript ‘M’ is another Earth-fixed frame (M-

frame), whose X-axis ( $X_M$ ) points to the magnetic North. The frame with the subscript ‘v’ is a moving frame attached to the vehicle (v-frame) and the frame of the subscript ‘s’ is another moving frame attached to the magnetometer (s-frame). Each frame is related to one another through yaw-pitch-roll angles. In the figure, roll and pitch angles are omitted for succinctness.

A magnetometer measures the Earth’s magnetic field in the s-frame. Since the Earth’s magnetic field is the constant vector pointing to the magnetic North in the M-frame, magnetometer measurements can be expressed by rotations of the magnetometer. By using the ZYX Euler angle definition (Fig. 2), the kinematic equation is obtained as

$$\begin{bmatrix} m_x \\ m_y \\ m_z \end{bmatrix} = \begin{bmatrix} \cos\psi_m \cos\theta_m & \sin\psi_m \cos\theta_m & -\sin\theta_m \\ -\sin\psi_m \cos\phi_m & \cos\psi_m \cos\phi_m & \cos\theta_m \sin\phi_m \\ +\cos\psi_m \sin\theta_m \sin\phi_m & +\sin\psi_m \sin\theta_m \sin\phi_m & \cos\theta_m \sin\phi_m \\ \sin\psi_m \sin\phi_m & -\cos\psi_m \sin\phi_m & \cos\theta_m \cos\phi_m \\ +\cos\psi_m \sin\theta_m \cos\phi_m & +\sin\psi_m \sin\theta_m \cos\phi_m & \end{bmatrix} \begin{bmatrix} M_x \\ M_y \\ M_z \end{bmatrix} \quad (1)$$

where

$[m_x \ m_y \ m_z]^T$  The Earth magnetic field measured in the s-frame

$[M_x \ M_y \ M_z]^T$  The Earth magnetic field measured in the M-frame

$[\psi_m \ \theta_m \ \phi_m]$  Yaw, pitch, and roll angles of the magnetometer with respect to M-frame

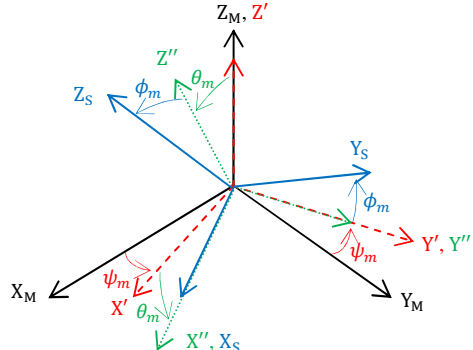


Fig. 2 ZYX Euler angles.  $\{X_M, Y_M, Z_M\}$  is the M-frame and  $\{X_s, Y_s, Z_s\}$  is the S-frame

As GPS velocity measurements are provided in the G-frame,  $(\psi + \psi_o, \theta + \theta_o, \phi + \phi_o)$  replace  $(\psi_m, \theta_m, \phi_m)$  where  $(\psi, \theta, \phi)$  are the Euler angles representing the vehicle attitude in the G-frame. The subscript ‘o’ means constant offset. For the yaw angle, the offset is a combination of a magnetometer mounting error and tilt of the magnetic North pole. For pitch and roll angles, offsets are purely from magnetometer mounting errors. These offsets are known values by calibration.

### B. Stochastic property of magnetic disturbances

Since the Earth’s magnetic field is weak ( $\approx 0.6$  Gauss), an adjacent vehicle can induce significant disturbances in magnetometer measurements [19-21]. Fig. 3 shows test data from a magnetometer collected during straight driving on a highway. The yaw angle is calculated by (1) assuming zero

pitch and roll angles. The yaw angle error at the 20 second mark was induced by a passing vehicle.

It is worth noting that the norm of the magnetometer measurement deviates from unity when a disturbance occurs. From 8 highway data sets, magnitude of the yaw angle error and the deviation of the magnetometer measurement from unity are plotted in Fig. 4. The correlation coefficient is 0.9, which suggests that deviation of the magnetic field norm is an effective indicator of magnetic disturbances.

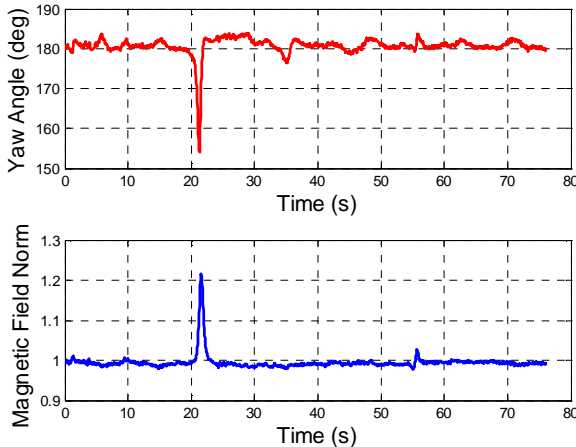


Fig. 3 Vehicle heading angle and magnetic field norm calculated from data collected during straight driving on a highway (I-96, Michigan)

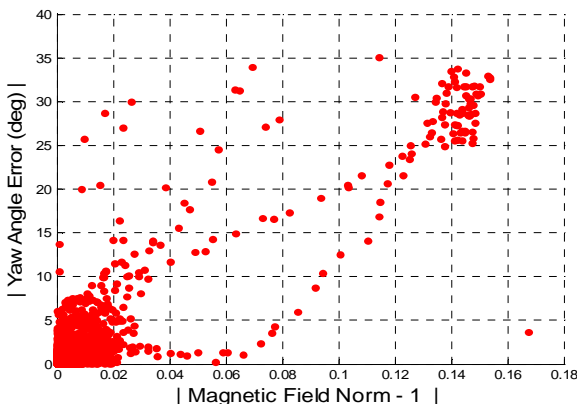


Fig. 4 A correlation plot between yaw angle error and deviation of magnetic field norm from unity. The yaw angle is calculated from magnetometer measurements only.

When the magnetic field norm deviates from unity more than a predefined threshold, the existence of magnetic field disturbance is detected. Let  $w$  be the magnitude of the disturbance. It is practical to assume that  $w$  does not reach infinity. Therefore, the absolute value of  $w$  is upper-bounded by a finite value  $b_o$ .  $w$  may be a function of magnetic strength of a disturbance source or distance between a magnetometer and a source. However, no prior knowledge of  $w$  is available when the disturbance is detected. Therefore, it is reasonable to assume that all the values of  $w$  inside  $b_o$  have the same probability. Consequently, the probability density function (PDF) of magnetic disturbance has a uniform distribution

bounded by  $b_o$ . In fact, Barmish rigorously justified the use of the uniform distribution when statistical information about the uncertain disturbance is unavailable [22] and some researchers adopted the same approach to handle disturbances [23-24].

### C. Optimal state estimation under disturbance: Scalar case

Let two random variables (r.v.)  $x$  and  $z$  be related via a joint probability density function  $f_{x,z}(x,z)$ . For any given measurement ( $z$ ), the optimal estimation of  $x$  minimizing  $\varepsilon[(x - \hat{x})^2]$  is

$$\hat{x} = \varepsilon(x|z) = \int_{-\infty}^{\infty} x \frac{f_{x,z}(x,z)}{f_z(z)} dx \quad (2)$$

where  $\varepsilon(\cdot)$  denotes the expected value. This is known as the minimum mean square error (MMSE) estimation. For the bivariate normal distribution, the optimal state estimate ( $\hat{x}$ ) is expressed as a linear function of measurement ( $z$ ).

A system of a disturbed measurement ( $z$ ) with the normally distributed state ( $x$ ) can be modeled as

$$\begin{aligned} x &= N(\mu_x, \sigma_x) \\ z &= cx + U(-b_o, b_o) \end{aligned} \quad (3)$$

where  
 $N, U$  the normal and uniform distribution, respectively  
 $\mu_x, \sigma_x$  mean and standard deviation of the r.v.  $x$   
 $c, b_o (\geq 0)$  correlation constant and bound of the r.v.  $z$

Then the MMSE estimation is

$$\hat{x}(z) = \int_{(z-b_o)/c}^{(z+b_o)/c} \left[ \frac{xe^{-\frac{1}{2}(\frac{x-\mu_x}{\sigma_x})^2}}{\int_{(z-b_o)/c}^{(z+b_o)/c} e^{-\frac{1}{2}(\frac{s-\mu_x}{\sigma_x})^2} ds} \right] dx \quad (4)$$

Equation (4) shows that the optimal state estimation has a nonlinear relationship with a measurement when the measurement is contaminated by unknown disturbances.

A linear relationship is preferred to be compatible with the Kalman Filter framework. To achieve this, the truncated normal distribution is used instead of the uniform distribution. It is a plausible approach because the truncated normal distribution can be a close approximation of the uniform distribution when the standard deviation is large enough compared to the truncated bound as seen in Fig. 5. In the figure, the truncated normal distribution whose standard deviation is ten times larger than the truncated bound resembles the uniform distribution.

Equation (5) shows the model of the joint normal and truncated normal distribution.

$$\begin{aligned} x &= N(\mu_x, \sigma_x) \\ z &= \begin{cases} \frac{\sigma_z}{\rho \sigma_x} x + N(0, \sigma_z) & \text{if } \left| z - \frac{\sigma_z}{\rho \sigma_x} x \right| \leq z_b \\ 0 & \text{otherwise} \end{cases} \end{aligned} \quad (5)$$

where  
 $\mu_x, \sigma_x$  mean and standard deviation of the r.v.  $x$   
 $\rho$  the correlation coefficient, which is  $\frac{\sigma_{xz}}{\sigma_x \sigma_z}$   
 $z_b, \sigma_z$  truncated bound and standard deviation of the r.v.  $z$

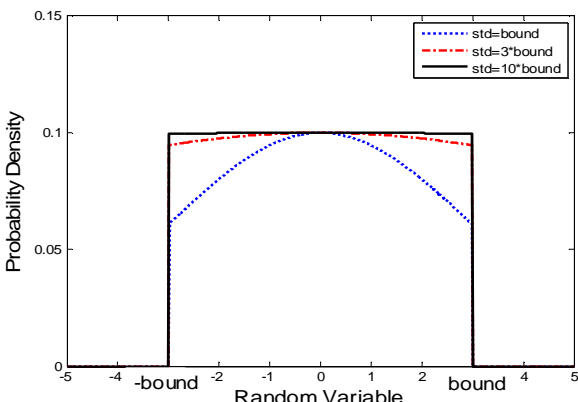


Fig. 5. Truncated Normal distributions with three different standard deviations. The Truncated Normal distribution whose standard deviation is ten times larger than the bound greatly resembles the Uniform distribution.

TABLE I  
STOCHASTIC PROPERTIES OF THE JOINT NORMAL AND TRUNCATED NORMAL DISTRIBUTION

$$\text{PDF } f_{X,Z}(x, z) = \begin{cases} A \exp\left(-\frac{1}{2(1-\rho^2)}\left[\left(\frac{x}{\sigma_x}\right)^2 - 2\rho\left(\frac{x}{\sigma_x}\right)\left(\frac{z}{\sigma_z}\right) + \left(\frac{z}{\sigma_z}\right)^2\right]\right), & |z - \frac{\sigma_z}{\rho\sigma_x}x| \leq z_b \\ 0, & \text{otherwise} \end{cases} \quad (6)$$

$$\text{where } A = \frac{1}{2\pi\sigma_x\sigma_z\sqrt{1-\rho^2}\left[\Phi\left(\frac{x_b}{\sigma_x\sqrt{1-\rho^2}}\right) - \Phi\left(\frac{-x_b}{\sigma_x\sqrt{1-\rho^2}}\right)\right]}$$

$$\Phi(x) = \int_{-\infty}^x \frac{1}{\sqrt{2\pi}} e^{-\frac{t^2}{2}} dt, \quad x_b = \rho \frac{\sigma_x}{\sigma_z} z_b$$

$$\text{MMSE } \hat{x} = \varepsilon(x|z) = \rho \frac{\sigma_x}{\sigma_z} z \quad (7)$$

$$\text{Variance } \iint_{-\infty}^{\infty} (z - \hat{z})^2 f_{X,Z}(x, z) dx dz = \sigma_z^2 (1 - \rho^2) m \quad (8)$$

$$\text{where } m = \left( \frac{1}{\Phi\left(\frac{z_b}{\sigma_z\sqrt{1-\rho^2}}\right) - \Phi\left(-\frac{z_b}{\sigma_z\sqrt{1-\rho^2}}\right)} + \frac{2 \frac{z_b}{\sigma_z\sqrt{1-\rho^2}} \Phi\left(\frac{z_b}{\sigma_z\sqrt{1-\rho^2}}\right)}{\left(\Phi\left(\frac{z_b}{\sigma_z\sqrt{1-\rho^2}}\right) - \Phi\left(-\frac{z_b}{\sigma_z\sqrt{1-\rho^2}}\right)\right)^2} \right)$$

$$\hat{z} = \frac{\sigma_z}{\rho\sigma_x} \hat{x}, \quad \varphi(x) = \frac{1}{\sqrt{2\pi}} e^{-\frac{1}{2}x^2}$$

Without loss of generality, the mean of random variable  $x$  ( $= \mu_x$ ) can be shifted to the origin. Then the joint PDF, MMSE estimation and the variance of the joint distribution are presented in Table 1 (See Appendix for details).

It is worth emphasizing that (7) and (8) are identical to those of the bivariate normal distribution except for the modification factor ( $m$ ) in (8). In other words, if a bivariate normal distribution has standard deviations of  $\sigma_x\sqrt{m}$  and  $\sigma_z\sqrt{m}$  respectively, its MMSE estimation and corresponding variance

would be same as (7) and (8). It should be noted that  $\sigma_z$  is not a statistical property. Instead, it is calculated from approximating the uniform distribution with the truncated normal distribution.

#### D. Optimal state estimation under disturbance: Vector case

The system and measurement equations are given as

$$x_k = \Phi_{k-1}x_{k-1} + \Gamma_{k-1}u_{k-1} + \Lambda_{k-1}w_{k-1} = \bar{x}_k + \Lambda_{k-1}w_{k-1} \quad (9)$$

$$z_k = H_k x_k + v_k \quad (10)$$

where

$x_k \in R^{n \times 1}$	State vector
$u_{k-1} \in R^{l_u \times 1}$	Input vector
$w_{k-1} \in R^{l_w \times 1}$	Plan error vector
$z_k \in R^{m \times 1}$	Measurement vector
$v_k \in R^{m \times 1}$	Measurement error vector
$\Phi_{k-1} \in R^{n \times n}$	State transition matrix
$\Gamma_{k-1} \in R^{n \times l_u}$	Input matrix
$\Lambda_{k-1} \in R^{n \times l_w}$	Plant noise matrix
$H_k \in R^{m \times n}$	Measurement matrix
$\bar{x}_k$	$\Phi_{k-1}x_{k-1} + \Gamma_{k-1}u_{k-1}$

Assume all the components of  $w_{k-1}$  in (9) are normally distributed with zero mean. Then,  $x_k$  in (9) is normally distributed around  $\bar{x}_k$ .

The  $i^{\text{th}}$  component of that measurement is

$$z_{i,k} = h_{i1,k}x_{1,k} + \dots + h_{in,k}x_{n,k} + v_{i,k} \equiv x_{G,k} + v_{i,k} \quad (11)$$

where

$h_{ij,k}$  (i,j) component of the measurement matrix  $H_k$  at time k

$x_{j,k}$  the j<sup>th</sup> component of the state  $x_k$  at time k

$v_{i,k}$  the i<sup>th</sup> component of the measurement error  $v_k$  at time k

$x_{G,k}$   $h_{i1,k}x_{1,k} + \dots + h_{in,k}x_{n,k}$

Since all the components of the state vector  $x_k$  are normally distributed, their linear combination ( $x_{G,k}$ ) is also normally distributed. If  $z_{i,k}$  is disturbed,  $x_{G,k}$  and  $z_{i,k}$  are

$$x_{G,k} = N(\bar{x}_{G,k}, \sigma_G) \quad (12)$$

$$z_{i,k} = x_{G,k} + U(-b_o, b_o)$$

where

$\bar{x}_{G,k}$  calculated with components of  $\bar{x}_k$

$\sigma_G$  Standard deviation of  $x_{G,k}$

$b_o$  The maximum bound of the disturbance

Since all the terms in (12) are scalar, (12) has exactly the same format as (3). By applying the lessons learned from the previous section, (12) is converted into

$$x_{G,k} = N(\bar{x}_{G,k}, \sigma_G \sqrt{m}) \quad (13)$$

$$z_{i,k} = x_{G,k} + N(0, \sigma_{i,z} \sqrt{m})$$

where

$\sigma_{i,z}$  Standard deviation of a truncated normal distribution of a disturbed measurement component ( $z_{i,k}$ )

$m$  The modification term calculated by (8)

Since  $\sqrt{m}$  is commonly applied to the standard deviations of the state and measurement, it will be cancelled out during the optimal state estimate calculation as seen in (7). Therefore, (14) yields the same state estimation as (13).

$$\begin{aligned} x_{G,k} &= N(\bar{x}_{G,k}, \sigma_G) \\ z_{i,k} &= x_{G,k} + N(0, \sigma_{i,z}) \end{aligned} \quad (14)$$

This result means that even a disturbed measurement can be treated with a normal distribution. Therefore the Kalman filter process can be applied here.

Given the system and measurement equations as (9) and (10), the Kalman Filter provides the optimal state estimation through (15)-(19) [25].

$$\hat{x}_k^- = \Phi_{k-1}\hat{x}_{k-1}^+ + \Gamma_{k-1}u_{k-1} \quad (15)$$

$$P_k^- = \Phi_{k-1}P_{k-1}^+\Phi_{k-1}^T + \Lambda_{k-1}\varepsilon(w_{k-1}w_{k-1}^T)\Lambda_{k-1}^T \quad (16)$$

$$K_k = P_k^- H_k^T [H_k P_k^- H_k^T + \varepsilon(v_k v_k^T)]^{-1} \quad (17)$$

$$\hat{x}_k^+ = \hat{x}_k^- + K_k(z_k - H_k\hat{x}_k^-) \quad (18)$$

$$P_k^+ = (I - K_k H_k)P_k^- \quad (19)$$

where

$\hat{x}_k^-(\hat{x}_k^+)$  The predicted (corrected) state estimate

$P_k^-(P_k^+)$  The predicted (corrected) state error covariance

Equations (15)-(16) produce the “time update” and (18)-(19) produce the “measurement update”.

It should be noted that  $\sigma_{i,z}$  is not a statistical property. Instead, it is set to make the truncated normal distribution mimic a uniform distribution and is intended to be much larger (at least ten times) than the truncated bound of disturbances. Let  $\sigma_{i,z,noise}$  be the standard deviation of the  $i^{\text{th}}$  measurement error component when undisturbed, then  $\eta_i$  is defined as

$$\eta_i \equiv \frac{\sigma_{i,z}}{\sigma_{i,z,noise}} \quad (20)$$

If the  $i^{\text{th}}$  measurement component is disturbed,  $\varepsilon(v_k v_k^T)$  of (17) is

$$\begin{bmatrix} \sigma_{1,z,noise}^2 & & & \\ & \ddots & & \\ & & \sigma_{i,z,noise}^2 & \\ & & & \ddots \\ & & & & \sigma_{m,z,noise}^2 \end{bmatrix} \begin{bmatrix} 1 & & & \\ & \ddots & & \\ & & \eta_i^2 & \\ & & & \ddots \\ & & & & 1 \end{bmatrix} = RM \quad (21)$$

Each measurement error component is assumed to be uncorrelated with each other. If measurements are not disturbed, the modification matrix ( $M$  of (21)) will be the identity matrix.

In summary, the existence of magnetic disturbance is detected by monitoring the norm of the magnetic field and those disturbances in measurements are addressed by introducing a modification matrix  $M$  in (21).

### III. DUAL KALMAN FILTERS

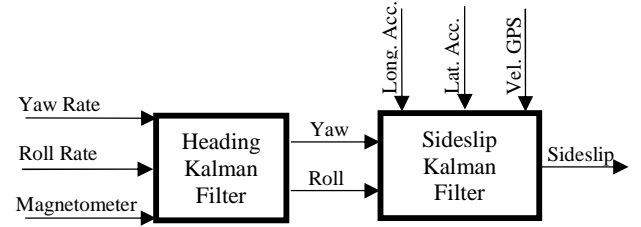


Fig. 6. Schematic diagram of the dual Kalman Filters

Fig. 6 shows the schematic overview of two Kalman Filters to estimate the vehicle sideslip angle. The Heading Kalman Filter yields yaw and roll angles by processing angular rate measurements of the IMU and magnetic field measurements. Then the vehicle sideslip is calculated through the Sideslip Kalman Filter by combining vehicle velocities measured by a single GPS receiver and vehicle accelerations from an IMU.

#### A. The Heading Kalman Filter

Recall that the magnetic field measurement contains yaw, pitch, and roll angles of a vehicle in the G-frame as (1) shows. At each data sampling, the magnetometer provides only one directional vector. However, to fully determine the attitude of a three-dimensional object, at least two independent directional vectors are required. Therefore the solution of (1) would have redundant answers. To resolve this redundancy concern, the pitch angle is assumed to be negligible. With this assumption, (1) is converted into (22), which is used as the measurement update equation of the Heading Kalman Filter.

$$g(\psi, \phi) = \begin{bmatrix} m_x \\ m_y \\ m_z \end{bmatrix} = \begin{bmatrix} M_x \cos \psi_m & -M_z \theta_o \\ -M_x \sin \psi_m \cos \phi_m + M_x \theta_o \cos \psi_m \sin \phi_m & M_z \sin \phi_m \\ M_x \sin \psi_m \sin \phi_m + M_x \theta_o \cos \psi_m \cos \phi_m & M_z \cos \phi_m \end{bmatrix} \quad (22)$$

where

$$\begin{bmatrix} \psi_m & \phi_m \end{bmatrix} \quad [\psi + \psi_o \quad \phi + \phi_o]$$

$[\psi_o \quad \phi_o \quad \theta_o]$  Constant offsets in angles

The pitch offset ( $\theta_o$ ) is assumed to be small.

Since (22) is nonlinear, the Extended Kalman Filter is used. Hence,  $H_k$  of (17) is replaced by the Jacobian of (22) with respect to the state  $(\hat{\psi}_k^-, \hat{\phi}_k^-)$  and  $g(\hat{\psi}_k^-, \hat{\phi}_k^-)$  substitutes for  $H_k \hat{x}_k^-$  of (18). The vector  $(\hat{\psi}_k^-, \hat{\phi}_k^-)$  is the predicted state estimate through the time update.

For the time update equation, the kinematics of angular rates and angles are employed as

$$\begin{bmatrix} \dot{\psi} \\ \dot{\phi} \end{bmatrix} = \begin{bmatrix} 0 & 0 \\ 0 & 0 \end{bmatrix} \begin{bmatrix} \psi \\ \phi \end{bmatrix} + \begin{bmatrix} r_m - b_r \\ p_m - b_p \end{bmatrix} + \text{noise} \quad (23)$$

where

$[r_m \quad p_m]$  yaw rate and roll rate measurements

$[b_r \quad b_p]$  biases in yaw rate and roll rate measurements

$\text{noise}$  Gaussian white noise

The state does not contain pitch angle due to the zero pitch assumption. The yaw rate and roll rate biases can be calculated during vehicle standstill.

### B. The Sideslip Kalman Filter

In the ISO coordinate system, the kinematics relating accelerations and velocities are

$$\begin{aligned} a_{x,m} &= \dot{U} - \dot{\psi}V + b_x + w_x \\ a_{y,m} &= \dot{V} + \dot{\psi}U + b_y + g\sin\phi + w_y \end{aligned} \quad (24)$$

where

$[a_{x,m} \ a_{y,m}]$	longitudinal/ lateral acceleration measurements
$[U \ V]$	longitudinal/lateral velocities
$[b_x \ b_y]$	biases in $[a_{x,m} \ a_{y,m}]$
$g\sin\phi$	gravitational component by roll
$[w_x \ w_y]$	the Gaussian white noise

As the yaw rate ( $\dot{\psi}$ ) is obtained by subtracting the yaw rate bias from the yaw rate measurements, (24) is rearranged to form the time update equation as (25). The accelerometer biases are augmented into the states to be estimated.

$$\begin{bmatrix} \dot{U} \\ \dot{b}_x \\ \dot{V} \\ \dot{b}_y \end{bmatrix} = \begin{bmatrix} 0 & -1 & \dot{\psi} & 0 \\ 0 & 0 & 0 & 0 \\ -\dot{\psi} & 0 & 0 & -1 \\ 0 & 0 & 0 & 0 \end{bmatrix} \begin{bmatrix} U \\ b_x \\ V \\ b_y \end{bmatrix} + \begin{bmatrix} 1 & 0 \\ 0 & 0 \\ 0 & 1 \\ 0 & 0 \end{bmatrix} \begin{bmatrix} a_{x,m} \\ a_{y,m} - g\sin\phi \end{bmatrix} + \text{noise} \quad (25)$$

A single antenna GPS can provide the vehicle velocity in the G-frame. As the vehicle heading is known from the Heading Kalman Filter, vehicle velocity measurement in the G-frame can be converted into longitudinal, lateral and vertical velocities via

$$\begin{bmatrix} U_{GPS} \\ V_{GPS} \\ V_{ver} \end{bmatrix} = \begin{bmatrix} \cos\psi & \sin\psi & 0 \\ -\cos\phi\sin\psi & \cos\phi\cos\psi & \sin\phi \\ \sin\phi\sin\psi & -\sin\phi\cos\psi & \cos\phi \end{bmatrix} \begin{bmatrix} V_N^{GPS} \\ V_W^{GPS} \\ V_U^{GPS} \end{bmatrix} \quad (26)$$

where

$[V_N^{GPS} \ V_W^{GPS} \ V_U^{GPS}]$	GPS velocities in the G-frame [North, West, Upward]
$[U^{GPS} \ V^{GPS} \ V_{ver}^{GPS}]$	GPS velocities in the v-frame [longitudinal, lateral, vertical]

Accordingly, when GPS velocity measurements are available, the measurement update equations are

$$\begin{bmatrix} U_{GPS} \\ V_{GPS} \end{bmatrix} = \begin{bmatrix} 1 & 0 & 0 & 0 \\ 0 & 0 & 1 & 0 \end{bmatrix} \begin{bmatrix} U \\ b_x \\ V \\ b_y \end{bmatrix} + \text{noise} \quad (27)$$

Once estimations of longitudinal and lateral velocities are obtained, sideslip angle is given by

$$\hat{\beta} = \tan^{-1}\left(\frac{\bar{v}}{\bar{u}}\right) \quad (28)$$

where  $\hat{\beta}, \bar{u}, \text{and } \bar{v}$  are estimations of sideslip angle, longitudinal velocity, and lateral velocity by the Sideslip Kalman Filter.

The velocity measurement by a low-cost GPS receiver is known to have a significant delay [15-17]. To address this issue, the idea of “measurement shifting” is borrowed from Larsen [26]. Fig. 7 shows a discrete time Kalman Filter framework to address delays. From time step  $s$  to  $k$ , state and its covariance are evolved only through time update because GPS measurements are unavailable. At time step  $k$ , the GPS velocity measurement is available ( $z_k$ ), but it represents a velocity of time step  $s$  due to the delay. Hence,  $z_k$  is shifted back to time step  $s$  and merged with the state estimation of  $\hat{x}_s$  to yield the measurement updated state ( $\hat{x}_s^{new}$ ). Then the updated state estimation at time step  $k$  ( $\hat{x}_k^{new}$ ) is obtained through the time update from  $\hat{x}_s^{new}$ .

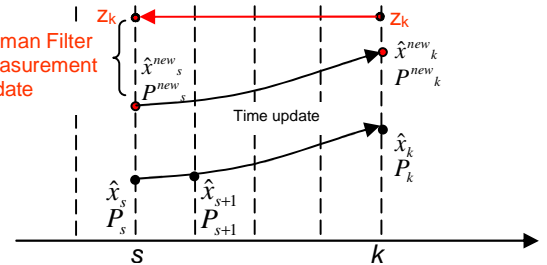


Fig. 7. Discrete Kalman Filter framework to handle delays

The GPS delay must be known to apply the “measurement shifting” technique. When a vehicle accelerates (or decelerates) during straight driving, the delay in GPS velocity measurements can be observed by comparing it to the vehicle velocity calculated from the wheel speed sensors. Hence the GPS delay is calculated during that maneuver. The vehicle acceleration (or deceleration) must be mild enough to avoid an excessive longitudinal wheel slip. As long as the delay varies at low frequency, it would be robustly estimated.

### IV. STOCHASTIC OBSERVABILITY ANALYSIS

Even though the Kalman Filter is capable of extracting optimal state estimations from noisy measurements, optimality does not imply stability. For linear time invariant (LTI) systems, the necessary and sufficient condition for the stability was identified in a clear form [27]. For time varying systems, however, only sufficient conditions were developed by Dyest, Price and Sorenson [28-29] and those are summarized in Jazwinski's book [30].

The system of (9)-(10) is said to be *uniformly completely observable* if there exists a positive integer  $N_o$  and positive constants  $\alpha_o, \beta_o$  such that

$$0 < \alpha_o I \leq O(k, k - N_o) \leq \beta_o I, \quad \forall k \geq N_o \quad (29)$$

where

$$\begin{aligned} O(k, k - N_o) &\equiv \sum_{i=k-N_o}^k \Phi_{i,k}^T H_i^T \varepsilon(v_i v_i^T)^{-1} H_i \Phi_{i,k} \\ \Phi_{k,i} &= \Phi_{k-1} \Phi_{k-2} \cdots \Phi_i, \quad \Phi_{k,k} = I, \text{ and } \Phi_{i,k} = (\Phi_{k,i})^{-1} \end{aligned}$$

The same system is said to be *uniformly completely controllable* if there exists a positive integer  $N_c$  and positive constants  $\alpha_c, \beta_c$  such that

$$0 < \alpha_c I \leq C(k, k - N_c) \leq \beta_c I, \quad \forall k \geq N_c \quad (30)$$

Where

$$C(k, k - N_c) \equiv \sum_{i=k-N_c}^{k-1} \Phi_{k,i+1} \Gamma_i \varepsilon(w_i w_i^T) \Gamma_i^T \Phi_{k,i+1}^T$$

For two symmetric matrices A and B,  $A \geq B$  means that  $(A-B)$  is positive semi-definite. If the system of (9)-(10) is uniformly completely observable, uniformly completely controllable, and the initial state error covariance matrix ( $P_0$ ) is greater than 0, then  $P_k^+$  of (19) is uniformly bounded from above and below

$$0 < [O + C^{-1}]^{-1} \leq P_k^+ \leq O^{-1} + C \quad \forall k \geq N \quad (31)$$

where

$$O = O(k, k - N), C = C(k, k - N), N = \max(N_o, N_c)$$

Given conditions for (31) are satisfied, it is proven that the state estimation error is *bounded-input bounded-output* (BIBO) stable [30] and the system of (9)-(10) is said to be *stochastically observable* in the sense that state error covariance matrix ( $P_k^+$ ) is upper bounded.

The stochastic observability of the Heading Kalman Filter is analyzed by investigating three conditions for (31). Since the measurement equation is nonlinear, the Extended Kalman Filter is used for the analysis [31]. Since this is a time-varying system, the observability relies on trajectories of the state. Therefore the author used procedures as follow; (i) choose a maneuver, (ii) choose an integer  $N$ , (iii) build  $O(k, k - N)$  and  $C(k, k - N)$  and (iv) evaluate  $\{\alpha_o, \beta_o, \alpha_c, \beta_c\}$ .

Maneuvers of single lane change (SLC), double lane change (DLC), slalom (SLL), and J-turn are selected.  $N$  of 1, 2, and 3 are tried.

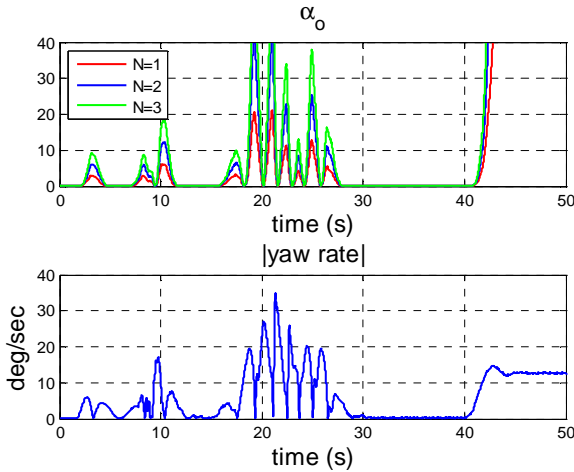


Fig. 8.  $\alpha_o$  and yaw rate absolute value

Since  $P_0$  is set to be greater than zero, the system is stochastically observable as long as all of  $\{\alpha_o, \beta_o, \alpha_c, \beta_c\}$  have positive values. In fact, they are positive regardless of  $N$  except for  $\alpha_o$ . Fig. 8 shows  $\alpha_o$  and corresponding absolute yaw rate values along the maneuvers. It is clearly observed that  $\alpha_o$  is positive only when the vehicle turns. Otherwise,  $\alpha_o$  stays at zero regardless of  $N$ . This suggests that the stochastic observability of the Heading Kalman Filter is guaranteed only when a vehicle turns. As the Sideslip Kalman Filter uses the yaw and roll angle estimations from the Heading Kalman

Filter, the stochastic observability of the Sideslip Kalman Filter is not guaranteed during straight driving either.

To resolve this observability concern of straight driving, the bicycle model is utilized. The bicycle model is a kinetic equation which describes vehicle lateral and yaw dynamics as seen in (32). Although the bicycle model requires accurate vehicle parameters in general, it can provide fairly accurate vehicle sideslip estimation during straight driving regardless of parameter accuracy. Fig. 9. shows the estimated sideslip by a bicycle model during a lane change on a snow covered road. Vehicle parameters including  $C_f$ ,  $C_r$ ,  $m$ , and  $I_z$  are manipulated to vary from 25% to 175% of nominal values.

$$\begin{bmatrix} \dot{\beta} \\ \dot{r} \end{bmatrix} = \begin{bmatrix} -\frac{C_f + C_r}{mU} & \frac{-l_f C_f + l_r C_r}{mU^2} - 1 \\ \frac{-l_f C_f + l_r C_r}{I_z} & \frac{l_f^2 C_f + l_r^2 C_r}{I_z U} \end{bmatrix} \begin{bmatrix} \beta \\ r \end{bmatrix} + \begin{bmatrix} \frac{C_f}{mU} \\ \frac{l_f C_f}{I_z} \end{bmatrix} \delta \quad (32)$$

where

$\beta$	vehicle sideslip angle
$r$	yaw rate
$m$	vehicle mass
$I_z$	moment of inertia with respect to the z axis
$\delta$	front axle steering angle
$C_f, C_r$	tire cornering stiffness (front and rear axle)
$l_f, l_r$	distance from vehicle center of mass to front and rear axles, respectively

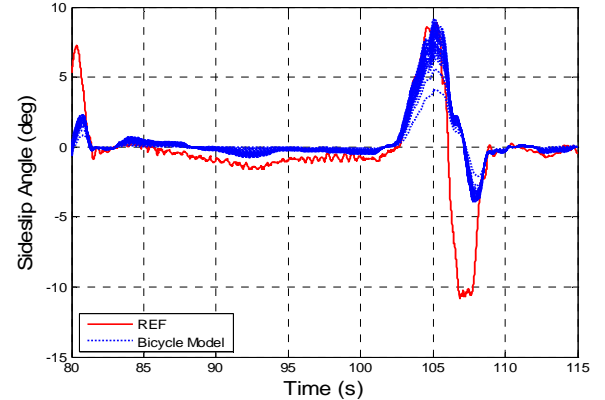


Fig. 9. The vehicle sideslip angle estimations by a bicycle model with parameters of 25%~175% of nominal values at 30 kph.

The red line is the true sideslip angle and blue lines represent estimations by the bicycle model with varied parameters. As seen in the figure, sideslip estimation is inaccurate during a lane change maneuver mainly due to the inaccurate tire cornering stiffness. However, it is worth emphasizing that sideslip is accurately estimated during straight driving regardless of parameter accuracy. Therefore the bicycle model is solely employed for sideslip estimation during straight driving. The straight driving is determined based on the vehicle yaw rate.

As the stochastic observability condition above is a sufficient condition, violating it does not necessarily mean “unobservable”. Unlike the Sideslip Kalman Filter, the Heading Kalman Filter does not have an effective alternative

during straight driving. Hence, the author keeps using the Heading Kalman Filter for the heading angle estimation even during the straight driving.

## V. SIMULATION RESULTS

Comprehensive simulations were run using Carsim<sup>TM</sup>, a popular tool for vehicle dynamics simulation and analysis. To cover various driving conditions, four types of maneuvers are combined with two friction types and two road bank types as listed in Table II. Fig. 10 shows the simulation layout. Black lines represent asphalt and cyan blue lines are ice surfaces. Solid lines are flat surfaces and dotted lines are banked surfaces. The total length of the road is 5.3 km. Various error sources shown in Table II are injected including biases in IMU, delay in GPS and random disturbances in a magnetometer.

TABLE II  
SIMULATION PROPERTIES

Simulation Properties	
Maneuver Type	Single Lane Change (SLC) Double Land Change (DLC) Slalom (SLL) J-Turn
Frictional Coefficient	0.8 for asphalt 0.3 for ice
Road Bank Type	0 deg for flat 5.71 deg (10%) for banked ice 8.53 deg (15%) for banked asphalt
Vehicle Type	Small size passenger car
Injected Error Properties	
IMU	Standard Deviation of White Noise 0.01 m/s <sup>2</sup> for acceleration 0.1 deg/s for rate gyros Injected Bias 0.5 m/s <sup>2</sup> for acceleration 2.0 deg/s for rate gyros
GPS	Standard Deviation of White Noise 0.01m/s Delay 400 ms
Magnetometer	Standard Deviation of White Noise 0.02 Disturbances 24 occurrences at random timing with random magnitude in [0.5, 2.0]

Fig. 11(a) shows deviations of the magnetic field norm from unity. Several peaks in the figure suggest simulated disturbances in the magnetic field. Fig. 11(b) and Fig. 11(c) show that yaw and roll angles are accurately estimated even though the magnetic field measurements are intermittently disturbed.

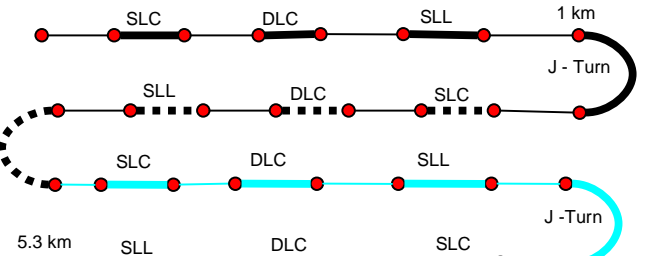


Fig. 10. The layout of the simulation “test track”

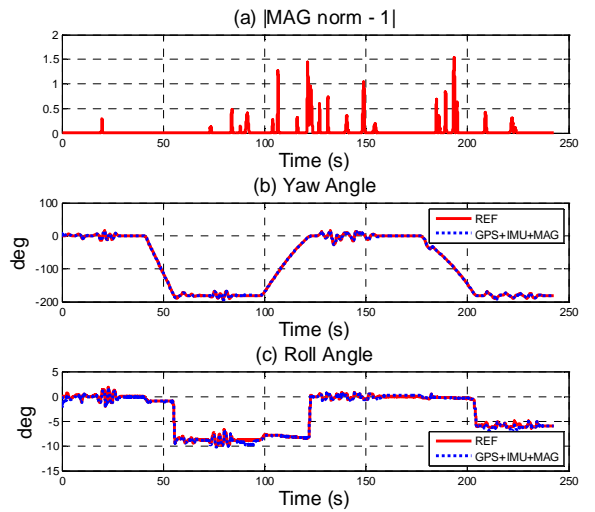


Fig. 11. Simulation results; (a) deviation of magnetic field norm due to injected disturbances, (b) yaw angle estimation, and (c) roll angle estimation.

Sideslip angle estimation performance of four selected road segments is presented in Fig. 12. The first 10 seconds of Fig. 12(a) shows considerable errors due to initialization. However, once initialization is completed, sideslip angle estimation stays close to the true values. Fig. 12(a) and Fig. 12(c) prove that the proposed method can yield accurate sideslip angle estimation at two considerably different surface frictions. Fig. 12(b) and Fig. 12(d) demonstrate that the method works even when a vehicle is on banked roads.

Equation (25) suggests that biases in lateral accelerometers are estimated. Unlike biases in the rate gyro, accelerometer bias estimation is a challenging problem because the gravity on a banked road would have the same effect on the accelerometer as biases. As the proposed method can estimate road bank angles, accelerometer biases are also calculated. For the verification, 0.5 m/s<sup>2</sup> offsets are injected in the accelerometer measurements and offsets of 8 m/s<sup>2</sup> are injected later for extreme case simulation. Two graphs in the Fig. 13 show that the proposed method estimates the injected biases successfully.

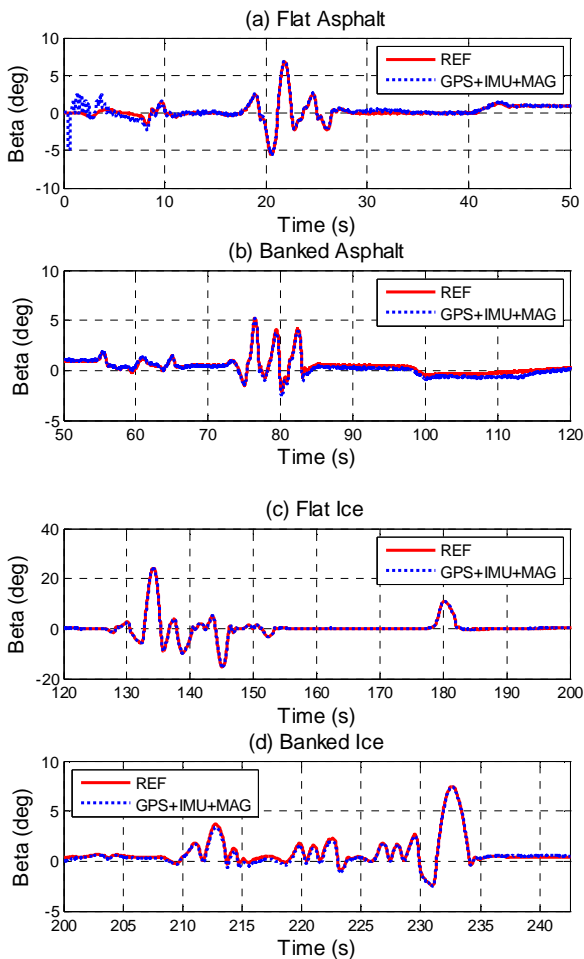


Fig. 12. The sideslip angle estimation performance on different friction and road bank levels; (a) flat asphalt, (b) banked asphalt, (c) flat ice, and (d) banked ice.

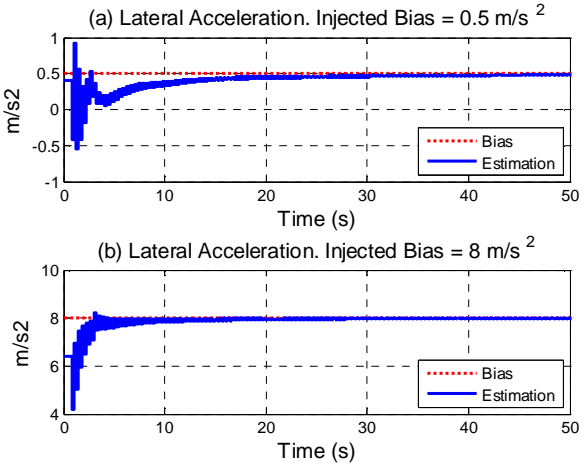


Fig. 13. Accelerometer bias estimation performance.

## VI. EXPERIMENTAL RESULTS

Experimental verification was conducted in two ways. One was to run pre-defined maneuvers on a test track, and the other was to drive the vehicle in a neighborhood area emulating daily driving. A GM Silverado pickup truck was equipped

with an Xsens MTi, an IMU from a production ESC unit, and an Oxford RT2500 (Fig. 14). The Xsens MTi provides three dimensional magnetic field measurements at 120 Hz sampling rate. The measurement noise level ( $1\sigma$ ) is 0.5 milli-Gauss. The IMU provides longitudinal/lateral accelerations and yaw rate at 166 Hz sampling rate. The measurement noise levels ( $1\sigma$ ) were  $0.02 \text{ m/s}^2$  and  $0.08 \text{ deg/sec}$  for accelerometer and rate gyro, respectively. The Oxford RT2500 provided the sideslip angle of its installed location at 100 Hz sampling rate. That sideslip angle was spatially translated to represent the vehicle sideslip angle at the center of gravity and is referred to as the reference signal hereinafter. The author used the vehicle velocity of the GPS receiver of the RT2500, whose measurement noise level ( $1\sigma$ ) is  $0.05 \text{ m/s}$ . To mimic the velocity signal of a low-cost GPS receiver, a 400 ms delay is injected and the data is down-sampled at 5 Hz from 100 Hz. The vehicle roll rate measurement was also provided by the Oxford RT2500. It was sampled at 100 Hz and measurement noise level ( $1\sigma$ ) was  $0.02 \text{ deg/sec}$ .



Fig. 14. Experimental setup on a test vehicle.

### A. On-Track Experiments

Four types of maneuvers including single lane change (SLC), double lane change (DLC), slalom (SLL) and J-Turn were run on packed snow and ice surfaces at the TRW winter test track in Raco, Michigan. Two different vehicle speeds representing fast (90 KPH on snow, 50 KPH on ice) and slow (60 KPH on snow, 30 KPH on ice) were executed. Each driving scenario had 5 runs; a total of 70 data sets (excluding J-turn on ice at slow speed) were collected. At each run, the vehicle followed the sequence of standstill (at least 5 sec), straight driving (at least 10 sec), and the testing maneuver

Fig. 15 shows typical traces of experimental data. Red lines are reference signals from RT2500, blue dotted lines are estimations by the proposed method, and the cyan blue areas are the 95% confidence range of the estimation. As seen in the figure, the sideslip estimation stays close to the reference signal. The sideslip RMS error from 70 collected runs is  $1.3^\circ$ . It was revealed that errors in sideslip estimation due to GPS noise grows as vehicle speed reduces [13]. The J-Turn maneuver resulted in significant vehicle speed reduction unlike other maneuvers. Consequently, the J-Turn shows a wider range of 95% confidence envelope at the end of the run

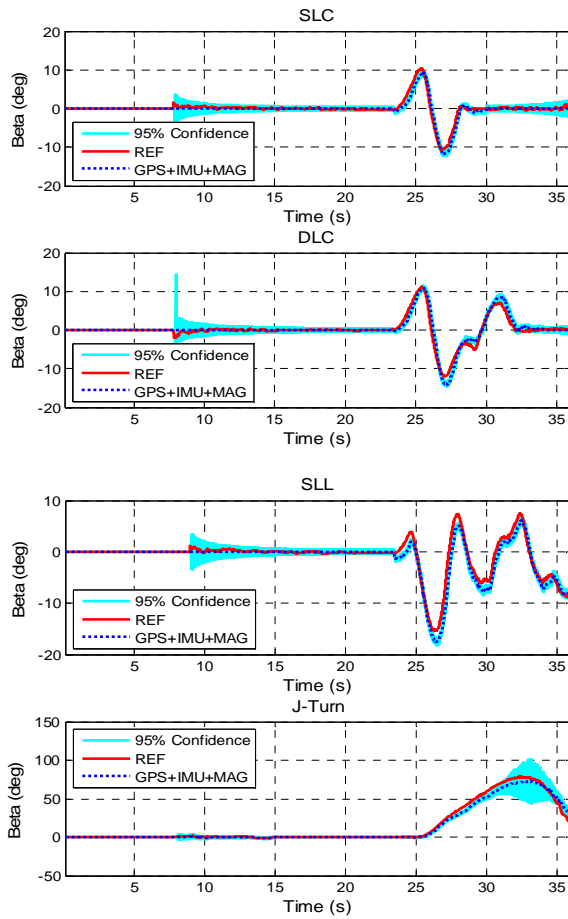


Fig. 15. The sideslip estimation performance of on-track experiments; (a) single lane change (SLC), (b) double lane change (DLC), (c) slalom (SLL), and (d) J-Turn

Since the test track had little magnetic disturbance, aforementioned performance does not prove the robustness of the algorithm against magnetic disturbances. To verify the magnetic disturbance rejection algorithm, randomly generated disturbances are injected into the on-track data. The disturbance of [0.05,1] at 20% was added, which means that the norm of randomly generated disturbance is between 0.05 and 1, and the disturbance takes 20% of total running time. This property is chosen to mimic actual disturbances based on collected highway data. With the injected disturbances, the sideslip RMS error from 70 data sets becomes  $1.98^\circ$ , which is about 50% higher than the magnetic disturbance-free data.

The impact of magnetic disturbance is studied further. A representative data of each maneuver (SLC, DLC, SLL and J-Turn) is selected and the data is processed twenty times with randomly generated magnetic disturbances of various magnitude and occurrence rates. Fig. 16 shows the outcome of SLC and SLL with the magnetic disturbance of [0.05,1] at 20%. Blue lines are the sideslip estimations by the proposed method where green dotted lines are the estimation without the disturbance rejection algorithm. The results with disturbance rejection stays close to the reference signal and the results without disturbance rejection are far worse, demonstrating the robustness of the proposed method against magnetic

disturbances. The sideslip RMS error from 80 runs (4 selected data  $\times$  20 runs) with the disturbance of [0.05,1] at 20% is  $1.28^\circ$ . Table 3 shows the sideslip RMS errors with different types of disturbance. When the occurrence rate is 20%, the disturbance has negligible effect. However, RMS error increases to  $2.23^\circ$  with 40% occurrence rate, which is 75% worse.

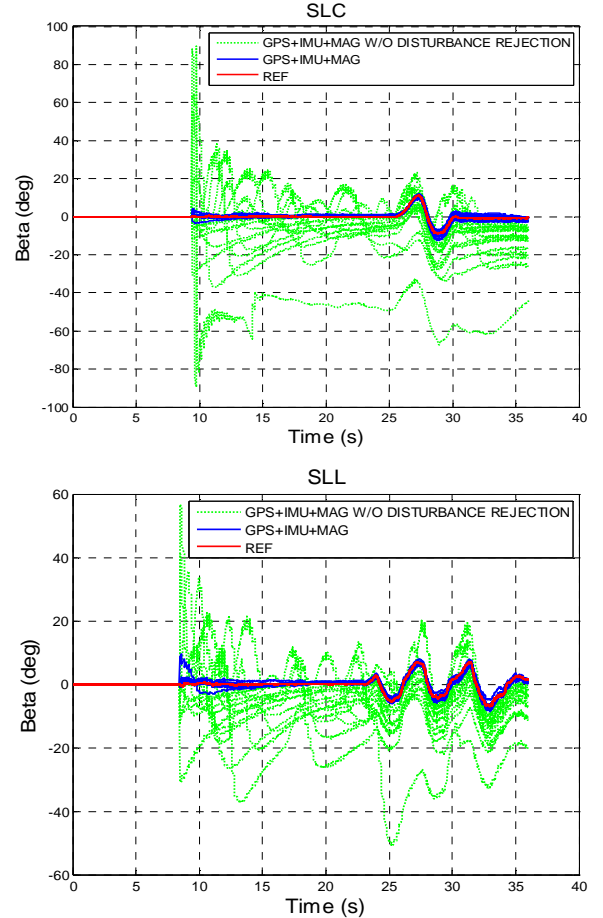


Fig. 16. The sideslip estimation performance of on-track experiments with and without magnetic disturbance rejection. Results from 20 runs with disturbance of [0.05,1]. Maneuvers of single lane change (SLC) and slalom (SLL) are shown.

TABLE III  
THE PERFORMANCE WITH DIFFERENT DISTURBANCE LEVELS

Disturbance Type	Sideslip RMS error
[0.01,0.015] at 20 %	$1.05^\circ$
[0.05,1] at 20 %	$1.28^\circ$
[1,2] at 20 %	$1.22^\circ$
[0.05,1] at 40 %	$2.23^\circ$

#### B. Neighborhood Area Experiments

The test vehicle was driven on neighborhood areas of Kinross, Michigan on February 25<sup>th</sup>, 2012. Fig. 17 shows the top view of the area. On that day, all the roads were covered with packed snow. Magnetic disturbance sources including

passing vehicles, houses, and utility poles with electric transformers were present in the area. A total of 9 data sets were collected and each run is 2 to 3 minutes long. Fig. 18 shows an example trace of steering angle, yaw rate and vehicle speed to give an idea of the driving maneuvers. Several aggressive cornering maneuvers were tried to create considerable sideslip angles on snow covered roads.



Fig. 17. Top view of the neighborhood area used for test (Kinross, Michigan)

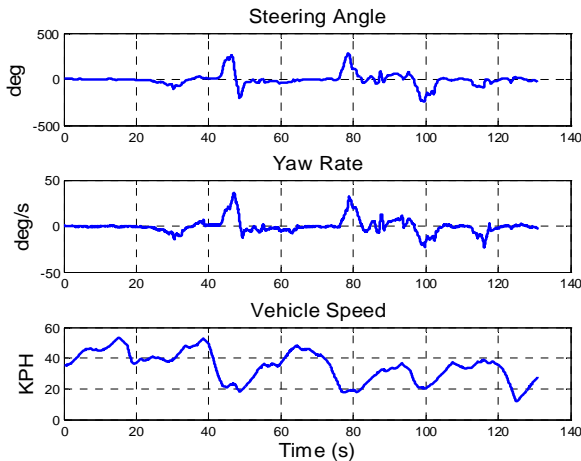


Fig. 18. An example of steering angle, yaw rate, and vehicle speed during neighborhood area experiments.

Fig. 19 provides three representative traces of neighborhood driving tests. Again, red lines are reference signals from RT2500, blue dotted lines are estimations by the proposed method and the cyan blue areas are the 95% confidence range of the estimation. Around the 13 second time mark of the first graph, 95% confidence range was exceptionally wider than others due to the slow vehicle speed. Overall, the estimation follows the reference signal successfully. However, the sideslip RMS error from 9 collected runs is  $2.45^\circ$ , which is worse than the simulations or on-track data.

This performance degradation can be explained by non-zero pitch angles. Fig. 20 (a) shows the vehicle pitch angles of the on-track (blue) and neighborhood area (red), measured by the Oxford RT 2500. The x-axis (time) is normalized for direct comparison. As can be seen, the neighborhood area had several segments of pitched roads. If the vehicle is on a pitched road, it would be recognized as a banked road in the proposed method due to zero pitch assumption. Erroneous roll

estimation would induce the sideslip estimation error because removal of roll gravitational effect from lateral measurements would be erroneous.

Noisier magnetic field may be another root-cause of the performance degradation. Fig. 20 (b) shows the magnetic field norm deviation of the on-track (blue) and neighborhood area (red). The neighborhood area shows more fluctuations than the on-track suggesting noisier magnetic field.

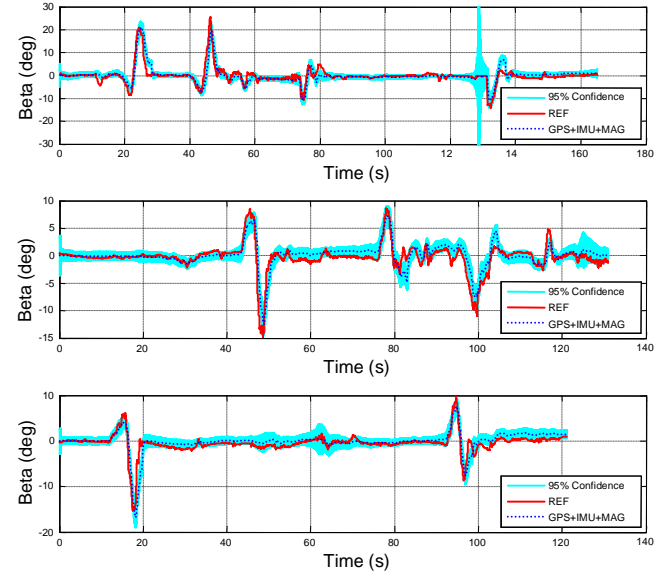


Fig. 19. The sideslip estimation performance of neighborhood area experiments; three representative plots.

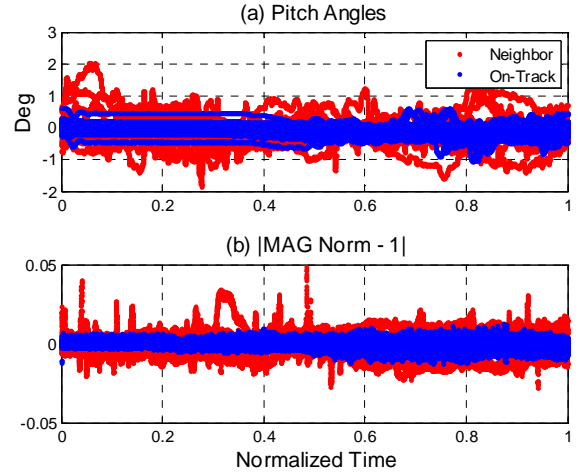


Fig. 20. Error sources of neighborhood area experiment data.

## VII. DISCUSSION

This paper has shown that the vehicle sideslip angle can be estimated by combining measurements of GPS, IMU and a magnetometer. The usefulness of magnetometers for ground vehicle applications was highly questioned due to its high susceptibility to large errors. However, this paper has shown the feasibility of a magnetometer for ground vehicle applications by introducing a disturbance rejecting stochastic

filter. As a result, the vehicle sideslip angle is robustly estimated regardless of surface friction and road bank angles.

Even though the dual-antenna GPS based method can achieve the same performance, the implementation cost of the proposed method is much lower. It is mainly because the proposed method utilizes GPS velocity only. The effectiveness of velocity measurement from a standard low-cost GPS was verified by Bevly [13]. The market survey by the author revealed that the velocity measuring performance has little correlation with the unit price (Fig. 21). As a result, the cheapest GPS receiver can be employed (The author found \$200 GPS development kit). Magnetometers are available in the price range of \$10-\$30 and low-cost IMU units are available from \$20 to \$50. Furthermore, these prices are for off-the-shelf products. If mass production is involved, it is assumed that the cost will drop further. Compared to dual antenna GPS modules whose price span in several thousand dollar range, the proposed method provides a cheaper option.

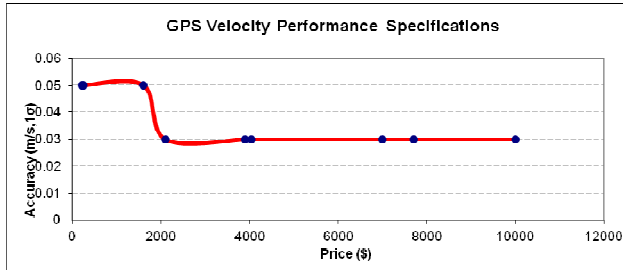


Fig. 21. GPS velocity performance vs. price. Integrated development kits of Novatel, NavSync and VBox are compared.

This paper assumes zero vehicle pitch angle to avoid redundancy issue of solving (1). Even though this method has been experimentally verified, the sideslip estimation accuracy is not guaranteed if pitch angles are significant. Therefore addressing significant vehicle pitch angle is a major future work of this paper.

## APPENDIX

### THE MMSE ESTIMATION AND THE VARIANCE OF THE JOINT NORMAL AND TRUNCATED NORMAL DISTRIBUTION

The PDF of the joint normal and truncated normal distribution (Equation (6)) is rewritten to (33) by converting the bound of r.v.  $z$  into r.v.  $x$

$$\begin{cases} A \exp\left[-\frac{1}{2(1-\rho^2)}\left(\left(\frac{x}{\sigma_x}\right)^2 - 2\rho\left(\frac{x}{\sigma_x}\right)\left(\frac{z}{\sigma_z}\right) + \left(\frac{z}{\sigma_z}\right)^2\right]\right] & \text{where } |x - x_o| < x_b \\ 0 & \text{otherwise} \end{cases} \quad (33)$$

$A$  is a constant to be determined and  $x_o \equiv \rho \frac{\sigma_x}{\sigma_z} z$  and  $x_b \equiv \rho \frac{\sigma_x}{\sigma_z} z_b$ . The optimal MMSE estimation is calculated by (2) as follows, where  $\Phi(x) = \int_{-\infty}^x \frac{1}{\sqrt{2\pi}} e^{-\frac{1}{2}t^2} dt$

$$\hat{x} = \varepsilon(x|z)$$

$$= \int_{x_o-x_b}^{x_o+x_b} \frac{A \exp\left(-\frac{1}{2}\left(\frac{z}{\sigma_z}\right)^2\right) \exp\left(-\frac{1}{2}\left(\frac{x-x_o}{\sigma_x\sqrt{1-\rho^2}}\right)^2\right)}{\int_{x_o-x_b}^{x_o+x_b} A \exp\left(-\frac{1}{2}\left(\frac{z}{\sigma_z}\right)^2\right) \exp\left(-\frac{1}{2}\left(\frac{s-x_o}{\sigma_x\sqrt{1-\rho^2}}\right)^2\right) ds} dx$$

$$\begin{aligned} &= \int_{-x_b}^{x_b} \frac{(t+x_o) \exp\left(-\frac{1}{2}\left(\frac{t}{\sigma_x\sqrt{1-\rho^2}}\right)^2\right)}{\int_{-x_b}^{x_b} \exp\left(-\frac{1}{2}\left(\frac{s'}{\sigma_x\sqrt{1-\rho^2}}\right)^2\right) ds'} dt \\ &= \int_{-x_b}^{x_b} \frac{(t+x_o) \exp\left(-\frac{1}{2}\left(\frac{t}{\sigma_x\sqrt{1-\rho^2}}\right)^2\right)}{\sqrt{2\pi(1-\rho^2)} \sigma_x \left\{ \Phi\left(\frac{x_b}{\sigma_x\sqrt{1-\rho^2}}\right) - \Phi\left(\frac{-x_b}{\sigma_x\sqrt{1-\rho^2}}\right) \right\}} dt \\ &= \frac{\int_{-x_b}^{x_b} t \exp\left(-\frac{1}{2}\left(\frac{t}{\sigma_x\sqrt{1-\rho^2}}\right)^2\right) dt + x_o \int_{-x_b}^{x_b} \exp\left(-\frac{1}{2}\left(\frac{t}{\sigma_x\sqrt{1-\rho^2}}\right)^2\right) dt}{\sqrt{2\pi(1-\rho^2)} \sigma_x \left\{ \Phi\left(\frac{x_b}{\sigma_x\sqrt{1-\rho^2}}\right) - \Phi\left(\frac{-x_b}{\sigma_x\sqrt{1-\rho^2}}\right) \right\}} \\ &= 0 + x_o \int_{-x_b}^{x_b} \frac{\exp\left(-\frac{1}{2}\left(\frac{t}{\sigma_x\sqrt{1-\rho^2}}\right)^2\right)}{\sqrt{2\pi(1-\rho^2)} \sigma_x \left\{ \Phi\left(\frac{x_b}{\sigma_x\sqrt{1-\rho^2}}\right) - \Phi\left(\frac{-x_b}{\sigma_x\sqrt{1-\rho^2}}\right) \right\}} dt \\ &= x_o \cdot 1 = \rho \frac{\sigma_x}{\sigma_z} z \end{aligned} \quad (34)$$

The constant  $A$  is calculated from  $\int_{-\infty}^{\infty} \int_{-\infty}^{\infty} f_{X,Z}(x,z) dx dz = 1$  as follows

$$\begin{aligned} &\int_{-\infty}^{\infty} \int_{-\infty}^{\infty} f_{X,Z}(x,z) dx dz \\ &= \int_{-\infty}^{\infty} \int_{x_o-x_b}^{x_o+x_b} A \exp\left\{-\frac{1}{2}\left(\frac{z}{\sigma_z}\right)^2\right\} \exp\left\{-\frac{1}{2}\left(\frac{x-x_o}{\sigma_x\sqrt{1-\rho^2}}\right)^2\right\} dx dz \\ &= A \sigma_x \sqrt{2\pi(1-\rho^2)} \left\{ \Phi\left(\frac{x_b}{\sigma_x\sqrt{1-\rho^2}}\right) - \Phi\left(\frac{-x_b}{\sigma_x\sqrt{1-\rho^2}}\right) \right\} \int_{-\infty}^{\infty} e^{-\frac{1}{2}\left(\frac{z}{\sigma_z}\right)^2} dz \\ &= 2\pi A \sigma_x \sigma_z \sqrt{(1-\rho^2)} \left\{ \Phi\left(\frac{x_b}{\sigma_x\sqrt{1-\rho^2}}\right) - \Phi\left(\frac{-x_b}{\sigma_x\sqrt{1-\rho^2}}\right) \right\} \\ &= 1 \\ \therefore A &= \frac{1}{2\pi \sigma_x \sigma_z \sqrt{(1-\rho^2)} \left\{ \Phi\left(\frac{x_b}{\sigma_x\sqrt{1-\rho^2}}\right) - \Phi\left(\frac{-x_b}{\sigma_x\sqrt{1-\rho^2}}\right) \right\}} \end{aligned} \quad (35)$$

The corresponding variance is calculated as follows, where  $\phi(x) = \frac{1}{\sqrt{2\pi}} e^{-\frac{1}{2}x^2}$

$$\begin{aligned} \text{variance} &= \int_{-\infty}^{\infty} \int_{-\infty}^{\infty} (x-x_o)^2 f_{X,Z}(x,z) dx dz \\ &= \int_{-\infty}^{\infty} \int_{x_o-x_b}^{x_o+x_b} A(x-x_o)^2 \exp\left\{-\frac{1}{2}\left(\frac{z}{\sigma_z}\right)^2\right\} \exp\left\{-\frac{1}{2}\left(\frac{x-x_o}{\sigma_x\sqrt{1-\rho^2}}\right)^2\right\} dx dz \\ &= \int_{-\infty}^{\infty} A \exp\left\{-\frac{1}{2}\left(\frac{z}{\sigma_z}\right)^2\right\} \int_{-x_b}^{x_b} x^2 \exp\left\{-\frac{1}{2}\left(\frac{x}{\sigma_x\sqrt{1-\rho^2}}\right)^2\right\} dx dz \\ &= \frac{\int_{-\infty}^{\infty} \frac{1}{\sqrt{2\pi}\sigma_z} \exp\left\{-\frac{1}{2}\left(\frac{z}{\sigma_z}\right)^2\right\} dz \int_{-x_b}^{x_b} \frac{x^2}{\sqrt{2\pi}\sigma_x\sqrt{1-\rho^2}} \exp\left\{-\frac{1}{2}\left(\frac{x}{\sigma_x\sqrt{1-\rho^2}}\right)^2\right\} dx}{\Phi\left(\frac{x_b}{\sigma_x\sqrt{1-\rho^2}}\right) - \Phi\left(\frac{-x_b}{\sigma_x\sqrt{1-\rho^2}}\right)} \\ &= \sigma_x \sqrt{1-\rho^2} \left[ \frac{1}{\Phi\left(\frac{x_b}{\sigma_x\sqrt{1-\rho^2}}\right) - \Phi\left(\frac{-x_b}{\sigma_x\sqrt{1-\rho^2}}\right)} + \frac{\frac{2x_b}{\sigma_x\sqrt{1-\rho^2}} \Phi\left(\frac{x_b}{\sigma_x\sqrt{1-\rho^2}}\right)}{\left\{ \Phi\left(\frac{x_b}{\sigma_x\sqrt{1-\rho^2}}\right) - \Phi\left(\frac{-x_b}{\sigma_x\sqrt{1-\rho^2}}\right) \right\}^2} \right] \end{aligned}$$

$$= \sigma_x \sqrt{1 - \rho^2} m$$

## ACKNOWLEDGMENT

The authors would like to thank TRW Automotive for providing the vehicle and facility for testing. Special thanks to Danny Milot of TRW Automotive for his encouragement and support, and Scott Floyd and Rick Ferrara for their technical advice.

## REFERENCES

- [1] J. Farrelly and P. Wellstead, "Estimation of Vehicle Lateral Velocity," in *IEEE International Conference on Control Applications*, Dearborn, MI, USA, 1996, pp. 552-557.
- [2] U. Kiencke and A. Daiss, "Observation of Lateral Vehicle Dynamics," *Control Engineering Practice*, vol. 5, pp. 1145-1150, 1997.
- [3] M. C. Best, *et al.*, "An Extended Adaptive Kalman Filter for Real-time State Estimation of Vehicle Handling Dynamics," *Vehicle System Dynamics*, vol. 34, pp. 57-75, 2000.
- [4] J. Stephan, *et al.*, "Virtual Sensor: Application to Vehicle Sideslip Angle and Transversal Forces," *IEEE Transactions on Industrial Electronics*, vol. 51, pp. 278-289, 2004.
- [5] H. Cherouat, *et al.*, "Vehicle velocity, side slip angles and yaw rate estimation," presented at the IEEE ISIE, Dubrovnik, Croatia, 2005.
- [6] P. Yih, *et al.*, "Vehicle State Estimation using Steering Torque," in *Proceeding of the 2004 American Control Conference*, Boston, Massachusetts, 2004.
- [7] X. Gao and Z. Yu, "Vehicle Sideslip Angle Estimation by using High Gain Observer," in *AVEC 9th International Symposium on Advanced Vehicle Control*, Kobe, Japan, 2008.
- [8] H. F. Grip, *et al.*, "Nonlinear Vehicle Side-Slip Estimation with Friction Adaptation," *Automatica*, vol. 44, pp. 611-622, 2008.
- [9] D. Piayabongkarn, *et al.*, "Development and Experimental Evaluation of A Slip Angle Estimator for Vehicle Stability Control," in *Proceeding of the 2006 American Control Conference*, Minneapolis, Minnesota, 2006.
- [10] T. D. Gillespie, *Fundamentals of Vehicle Dynamics*. Warrendale, PA: Society of Automotive Engineers, Inc., 1992.
- [11] L. Imsland, *et al.*, "Vehicle Velocity Estimation using Modular Nonlinear Observers," *Automatica*, vol. 42, pp. 2091-2103, 2006.
- [12] A. Y. Ungoren, *et al.*, "Experimental Verification of Lateral Speed Estimation Methods," in *AVEC 6th International Symposium on Advanced Vehicle Control*, Hiroshima, Japan, 2002.
- [13] D. M. Bevly, "Global Positioning System (GPS): A Low-Cost Velocity Sensor for Correcting Inertial Sensor Errors on Ground Vehicles," *Journal of Dynamic System, Measurement, and Control*, vol. 126, pp. 255-264, 2004.
- [14] D. M. Bevly, *et al.*, "The Use of GPS Based Velocity Measurements for Measurement of Sideslip and Wheel slip," *Vehicle System Dynamics*, vol. 38, pp. 127-147, 2003.
- [15] J.-H. Yoon and H. Peng, "Vehicle Sideslip Angle Estimation Using Two Single-Antenna GPS Receivers," in *Dynamic System Control Conference*, Boston, MA, 2010.
- [16] J. Ryu and J. C. Gerdes, "Integrating Inertial Sensors with GPS for Vehicle Dynamics Control," *Journal of Dynamic System, Measurement, and Control*, vol. 126, pp. 243-254, 2004.
- [17] J. Ryu, *et al.*, "Vehicle Sideslip and Roll Parameter Estimation Using GPS," in *AVEC 6th International Symposium on Advanced Vehicle Control*, Hiroshima, Japan, 2002.
- [18] J. Ryu and J. C. Gerdes, "Estimation of Vehicle Roll and Road Bank Angle," in *Proceeding of the 2004 American Control Conference*, Boston, Massachusetts, 2004.
- [19] E. Abbott and J. D. Powell, "Land-Vehicle Navigation Using GPS," in *Proceedings of the IEEE*, 1999, pp. 145-162.
- [20] P. Ripka, *Magnetic sensors and magnetometers*: Artech House, 2001.
- [21] S. Taghvaeeyan and R. Rajamani, (2001, Use of vehicle magnetic signatures for position estimation. *Applied Physics Letters* 99(134101).
- [22] B. R. Barmish and C. M. Lagoa, "The Uniform Distribution: A Rigorous Justification for its use in Robustness Analysis," *Mathematics of Control, Signals, and Systems*, vol. 10, pp. 203-222, 1997.
- [23] M. Prandini and M. C. Campi, "A new approach to controller design in presence of constraints," in *IEEE Conference on Decision and Control*, New Orleans, LA, USA, 2007.
- [24] M. L. Muhler and B. R. Barmish, "A Uniformity Principle for Probabilistic Robustness of the Discrete-Time Linear Quadratic Regulator," in *American Control Conference*, San Diego, CA, 1999.
- [25] M. S. Grewal and A. P. Andrews, *Kalman Filtering: Theory and Practice*: Prentice-Hall, Inc., 1993.
- [26] T. D. Larsen, *et al.*, "Incorporation of time delayed measurements in a Discrete-time Kalman Filter," in *Proceedings of the 37th IEEE conference on Decision & Control*, Tampa, Florida, 1998, pp. 3972-3977.
- [27] R. Stengel, *Optimal Control and Estimation*. New York: Dover Publications, Inc., 1994.
- [28] J. Deyst, John J. and C. F. Price, "Conditions for Asymptotic Stability of the Discrete Minimum-Variance Linear Estimator" *IEEE Transactions on Automatic Control*, vol. AC-13, pp. 702-705, 1968.
- [29] H. W. Sorenson, "On the Error Behavior in Linear Minimum Variance Estimation Problems," *IEEE Transactions on Automatic Control*, vol. 12, pp. 557-562, 1967.
- [30] A. H. Jazwinski, *Stochastic processes and filtering theory*. New York: Academic Press, 1970.
- [31] V. L. Bageshwar, *et al.*, "A Stochastic Observability Test for Discrete-Time Kalman Filters," *Journal of Guidance, Control, and Dynamics*, vol. 32, 2009.



**Jong-Hwa Yoon** received his B.S. degree from Seoul National University, South Korea, in 2002, and an M.S.E. degree from the University of Michigan, Ann Arbor, MI, USA, in 2004.

He is currently a Ph.D. degree candidate in mechanical engineering at the University of Michigan, Ann Arbor, MI, USA. His research interests include stochastic filter theory, optimal estimation, vehicle dynamics, vehicle active safety systems, and GPS technology. He is also associated with TRW Automotive, Livonia, MI, USA as senior engineer in System and Control Design Department.



**Huei Peng** received his Ph.D. from the University of California, Berkeley in 1992. He is currently a Professor at the Department of Mechanical Engineering at the University of Michigan. His research interests include adaptive control and optimal control, with emphasis on their applications to vehicular and transportation systems. His current research focuses include design and control of hybrid vehicles and vehicle active safety systems.

In the last 10 years, he was involved in the design of several military and civilian concept vehicles, including FTTS, FMTV, and Super-HUMMV—both electric and hydraulic hybrid vehicle concept designs. He is currently the US Director of the Clean Energy Research Center—Clean Vehicle Consortium, which supports 29 research projects related to the development and analysis of clean vehicles in US and China. He also leads an education project funded by DOE to develop 10 undergraduate and graduate courses including three laboratories courses focusing on transportation electrification. He has more than 200 technical publications, including 85 in referred journals and transactions.

Huei Peng has been an active member of the Society of Automotive Engineers (SAE) and the ASME Dynamic System and Control Division (DSCD). He served as the chair of the ASME DSCD Transportation Panel from 1995 to 1997, and is a member of the Executive Committee of ASME DSCD. He served as an Associate Editor for the IEEE/ASME Transactions on Mechatronics from 1998-2004 and for the ASME Journal of Dynamic Systems, Measurement and Control from 2004-2009. He received the National Science Foundation (NSF) Career award in 1998. He is an ASME Fellow. He is a ChangJiang Scholar at the Tsinghua University.